Chaos, Solitons and Fractals 200 (2025) 116966

Contents lists available at ScienceDirect

Chaos, Solitons and Fractals

journal homepage: www.elsevier.com/locate/chaos

Transport mechanisms associated with non-integer wavenumbers in a discontinuous nontwist map

Matheus Rolim Sales [a,b,*], Michele Mugnaine [c,d], Ana L.R. de Moraes [c], Edson Denis Leonel [b], Chris G. Antonopoulos [a,*], Iberê Luiz Caldas [c], José Danilo Szezech Jr. [c,e,f]

[a] University of Essex, School of Mathematics, Statistics and Actuarial Science, Wivenhoe Park, Colchester, CO4 3SQ, United Kingdom
[b] São Paulo State University (UNESP), Institute of Geosciences and Exact Sciences, 13506-900, Rio Claro, SP, Brazil
[c] Institute of Physics, University of São Paulo, 05315-970, São Paulo, SP, Brazil
[d] Lorena School of Engineering (EEL-USP), University of São Paulo, 12602-810, Lorena, SP, Brazil
[e] Graduate Program in Science, State University of Ponta Grossa, 84030-900, Ponta Grossa, PR, Brazil
[f] Department of Mathematics and Statistics, State University of Ponta Grossa, 84030-900, Ponta Grossa, PR, Brazil

ARTICLE INFO

Keywords:
Transport mechanism
Nontwist map
Stable and unstable manifolds

ABSTRACT

The transport properties in two-dimensional, area-preserving mappings are deeply influenced by the phase space structures such as invariant tori, cantori, and manifold crossings. For nontwist maps, the presence or absence of the shearless invariant curve dictates whether the map exhibits global transport. In this paper, we investigate the extended standard nontwist map, which consists of the standard nontwist map perturbed by a secondary wavenumber m. We explore the transport and behavior of chaotic orbits for arbitrary real m. Our results confirm that the twin island chain scenario only holds for odd integer m, and reveal that the probability of chaotic orbits crossing the central island chain is highly sensitive to m. We demonstrate that for certain m, the manifold configuration is such that only unidirectional transport is achieved, either upward or downward, or heteroclinic orbits from the primary resonances are suppressed entirely, significantly reducing the transport. Additionally, we identify a narrow interval of m for which the shearless curve reemerges, preventing transport altogether. Our findings are supported by detailed and high-precision numerical analysis of the stable and unstable manifolds and their intra and intercrossing structures.

1. Introduction

The dynamics of a two degrees-of-freedom Hamiltonian system can be reduced to the analysis of a two-dimensional, area-preserving mapping using energy conservation and an appropriate Poincaré section [1]. The phase space of a two-dimensional, area-preserving mapping is, in general, composed of both regular (periodic and quasi-periodic) and chaotic domains. In the integrable case, all initial conditions lie on periodic and quasi-periodic rotational invariant tori and as a weak perturbation is introduced to the map, the Kolmogorov–Arnold–Moser (KAM) theorem [1] establishes that the rational tori are destroyed while the sufficiently irrational ones survive weak perturbations (KAM tori). According to the Poincaré–Birkhoff theorem [1], a set of elliptic (centers) and hyperbolic (saddles) periodic orbits appears near the original location of the destroyed rational tori. The stability islands (quasi-periodic orbits) are formed around the elliptic points and it is the instability of the hyperbolic points that generates chaotic behavior.

* Corresponding authors.
E-mail addresses: rolim.sales.m@gmail.com (M. Rolim Sales), canton@essex.ac.uk (C.G. Antonopoulos).

https://doi.org/10.1016/j.chaos.2025.116966
Received 20 May 2025; Received in revised form 9 July 2025; Accepted 28 July 2025

The stability islands are foliated with KAM tori and in two-dimensional, area-preserving maps, these tori are barriers to the transport in phase space, making the regular and chaotic regions disjoint domains.

As the perturbation grows stronger, the KAM tori are also destroyed and their remnants form a Cantor set called cantori [2–4]. The cantori are robust partial transport barriers that, differently from the KAM tori, do not fully prevent the transport of orbits, but rather decrease it significantly. The chaotic orbits that enter a region bounded by a cantorus might stay trapped within this region for a long, but finite, period of time, during which they behave similarly to quasiperiodic orbits, until they escape to the chaotic sea. As a chaotic orbit evolves in time, it can repeatedly enter and exit regions bounded by the cantori, leading to intermittent behavior in its time evolution. This intermittence is the phenomenon of stickiness [4–14] and it affects some statistical properties such as the recurrence time statistics [15–20], survival probability [13,21–27], and decay of correlations [7,8,28,29]. It also increases the uncertainty for smaller length scales [30,31] and influences diffusion [32–35] and transport properties [15,36–40].

The stable and unstable manifolds of the hyperbolic periodic orbits, left behind from the destruction of the rational tori, bounding a set of elliptic centers form the boundary of a resonance zone [40–42]. These manifolds intersect repeatedly, generating a homoclinic tangle and creating a chain of contiguous lobes. Transport into and out of the resonance zone occurs through turnstiles, which are formed by pairs of adjacent lobes. Typically, the phase space of a two-dimensional, area-preserving mapping exhibits a hierarchical structure of islands-around-islands embedded in the chaotic sea. Each stability island is surrounded by a set of periodic elliptic orbits, which form smaller stability islands, which are in turn surrounded by even smaller stability islands, and so on and so forth for increasingly smaller scales [9,10]. The transport between these hierarchical levels is achieved through turnstiles and there are also smaller cantori between each resonance.

The existence of cantori in phase space has been rigorously proven only for nondegenerate Hamiltonian systems, i.e., those in which the frequency of the motion is a monotonic (non-vanishing derivative) function of the actions [1]. The nondegeneracy condition, also known as twist condition, for maps is defined as $\partial x_{n+1}/\partial y_n \neq 0$. Mappings that satisfy this condition in every point of phase space are called twist maps, whereas those that violate it at one or more points are called nontwist maps. One of the simplest mathematical models that violate the twist condition is the standard nontwist map (SNM) [43]. It has become a paradigmatic model for the study of nontwist maps for capturing the universal behavior of this kind of system.

Some analytical results using KAM theory have been obtained for nontwist systems [44], however most of the analysis has been done via numerical simulations [43,45–51], especially related to the transport of chaotic orbits [52–63]. In the case of the SNM, or any nontwist system where the frequency map depends quadratically on the action, the phase space is often composed of a chaotic domain with two island chains embedded in it. Due to the violation of the twist condition, the two island chains are twins, i.e, they have the same frequency but are different islands. In between the island chains, along the points where the twist condition is not satisfied, there is the shearless curve, located at the extremum of the nonmonotonic frequency. The shearless curve is a robust invariant curve that acts as a barrier to the transport of chaotic orbits. It divides the phase space into two distinct and unconnected domains and once this curve is broken, a single chaotic orbit fills the entire chaotic component of phase space, and global transport is achieved.

In nontwist systems, the shearless curve is the last invariant rotational curve to be destroyed. After its destruction, the only type of barriers in phase space are the partial barriers we have discussed. Additionally to that, the remnants of the shearless curve can also influence and trap chaotic orbits [52]. It has also been shown that the manifold structure plays a crucial role in the transport in phase space [54]. The intra-intercrossing scenario of the manifolds influences whether a high or low transport is observed and, more recently, it has been demonstrated the existence of an effective barrier of transport induced by island chains of even period in the SNM [59].

In this paper, we analyze the transport properties of the extended standard nontwist map (ESNM) [64,65], which extends the standard nontwist map (SNM) by including an additional perturbation term with a different wavenumber m. While previous studies have considered only integer values of m [55,64,65], we generalize the analysis to real-valued m. We demonstrate that the twin island chain scenario occurs only when m is an odd integer [55], and not for arbitrary real values. Furthermore, we find that the probability of chaotic orbits crossing the island chain depends sensitively on m, and that for certain values, the manifold configuration restricts transport to a single direction either upward or downward. This directional dependence is linked to the existence of two distinct types of heteroclinic tangles: upward and downward intercrossings. In some cases, we observe the absence of heteroclinic tangle between the primary resonance islands, resulting instead in an intracrossing tangle, which substantially suppresses transport and results in the formation of persistent barriers for very long times. Finally, we identify a narrow interval in m for which a shearless invariant curve reappears, completely inhibiting transport for all time.

This paper is organized as follows. In Section 2, we introduce the ESNM and briefly discuss some of its known properties. In Section 3, we discuss the mechanism behind the transport of chaotic orbits for real values of the wave-number m across the central chain of stability islands using the transmissivity as a quantifier of transport. We compute the stable and unstable manifolds of the corresponding hyperbolic orbits and analyze the intra-intercrossing scenarios and how they are related to the transmissivity. Section 4 contains our final remarks.

2. The model and its properties

A general two-dimensional, area-preserving mapping $\mathcal{M} : \mathbb{R}^2 \to \mathbb{R}^2$ can be described by the following equations [1]:

$$\begin{aligned} y_{n+1} &= y_n + \epsilon f(x_n), \\ x_{n+1} &= x_n + \Omega(y_{n+1}), \end{aligned} \tag{1}$$

where $\epsilon \geq 0$ is a perturbation, the function f is periodic in x with period 2π or unity, and $\Omega(y_{n+1})$ is the rotation number $\omega \equiv \omega(y)$ whose derivative is the shear. We call the mapping given by Eq. (1) *twist* if

$$\left|\frac{\partial x_{n+1}}{\partial y_n}\right| > 0 \tag{2}$$

for every value of (y_n, x_n). The condition given by Eq. (2) is the so-called twist condition and if it is not satisfied somewhere in phase space, we call the mapping *nontwist*. The twist condition is the shear condition, meaning the derivative of the rotation number satisfies $|\omega'(y)| > 0$. Consequently, the rotation number of a twist system is monotonic, either strictly increasing or strictly decreasing.

Suppose we choose $f(x_n) = \sin x_n$ and change $\Omega(y_{n+1})$. In that case, we obtain different interesting mappings, such as the Chirikov–Taylor standard map ($\Omega(y_{n+1}) = y_{n+1}$) [66], the Fermi–Ulam model ($\Omega(y_{n+1}) = 2/y_{n+1}$) [67,68], and the Leonel mapping ($\Omega(y_{n+1}) = |y_{n+1}|^{-\gamma}$) [26,32,69–71], to cite a few.

In this paper, we consider the extended standard nontwist mapping (ESNM) defined by the following equations [64,65]:

$$\begin{aligned} y_{n+1} &= y_n - b\sin(2\pi x_n) - c\sin(2\pi m x_n), \\ x_{n+1} &= x_n + a(1 - y_{n+1}^2) \bmod 1, \end{aligned} \tag{3}$$

where a, b, and c are real valued parameters and $\Omega(y_{n+1}) = a(1 - y_{n+1}^2)$. The parameter m was originally considered a positive integer number [64,65]. Our study, however, focuses on the ESNM considering $m \in \mathbb{R}$. The phase space of the ESNM is a cylinder defined as $(x, y) \in [0, 1) \times (-\infty, \infty)$ and the mapping is also called two-frequency standard nontwist map [65]. The parameter $a \geq 0$ is the profile parameter and $b \geq 0$ and $c \geq 0$ are the strengths of the two different perturbations. For $c = 0$, we recover the standard nontwist map (SNM) [43] and for $b = c = 0$, the system is integrable and every orbit lies on an invariant rotational torus.

It is important to mention that even though our forcing term $f(x) = -b\sin(2\pi x) - c\sin(2\pi m x)$ is continuous for $x \in \mathbb{R}$, when we take $x \bmod 1$, $f(x)$ becomes discontinuous on the interval $x \in [0, 1)$. The transport properties of chaotic trajectories in two-dimensional, discontinuous, dissipative maps have been investigated in Refs. [72–74], and similar studies have been done for discontinuous, area-preserving maps [75–77]. A particularly illustrative example of a discontinuous area-preserving map is provided by polygonal billiards [78], where the discontinuities are located at the corners of the billiard.

Regarding the periodicity of our forcing term, $f(x)$, it is periodic for rational m, but when m is irrational, the forcing becomes quasiperiodic. Quasiperiodic forcing has been used to study strange nonchaotic attractors in dissipative systems since the 1980s [79,80], however, to the best our knowledge, there has been no study focused only on the effect of a quasiperiodic forcing in area-preserving maps.

The ESNM violates the twist condition along an invariant curve in phase space called shearless curve. For the ESNM, the rotation number is $\Omega(y) = a(1 - y^2)$, and due to this quadratic dependence of $\Omega(y)$ on y, there exist two island chains with the same rotation number ω on both sides of the shearless curve. The shearless curve is a robust transport barrier that separates the phase space into distinct and unconnected domains. The transition to global stochasticity due to the destruction of the shearless curve has been studied in both the SNM [46,47,81] and the ESNM [55] as well as the mechanism of transport in the SNM [52,54] and the identification of effective barriers that persist after the shearless curve destruction [53,59].

del-Castillo-Negrete et al. showed that the SNM [$c = 0$ in Eq. (3)] is symmetric over the following symmetry transformation [46]:

$$\mathcal{T} = (x \pm \frac{1}{2}, -y). \tag{4}$$

With this transformation, given a regular orbit with rotation number ω, we find a different regular orbit with the same rotation number ω, i.e., given an island chain, we find the other chain by applying this transformation. A mapping $\mathcal{M}$ is said to be symmetric over a transformation $\mathcal{T}$ if $\mathcal{M}$ satisfies $\mathcal{T}\mathcal{M} = \mathcal{M}\mathcal{T}$. Thus, we can check whether the ESNM is also symmetric over the transformation $\mathcal{T}$ given by Eq. (4). We find the following identities:

$$\begin{aligned} &(x \pm \frac{1}{2}) + a(1 - y^2) = [x + a(1 - y^2)] \pm \frac{1}{2}, \\ &-\ y + b\sin(2\pi x) - c\sin(2\pi m x \pm m\pi) = \\ &= -y + b\sin(2\pi x) + c\sin(2\pi m x). \end{aligned} \tag{5}$$

The first identity is satisfied for all values of x and y. The second identity, on the other hand, requires a deeper analysis. Expanding the third term on the left-hand side, we obtain

$$-\sin(2\pi m x)\cos(m\pi) \pm \cos(2\pi m x)\sin(m\pi) = \sin(2\pi m x).$$

For the case of integer m, either positive or negative, we obtain $\sin(m\pi) = 0$ and $\cos(m\pi) = (-1)^{|m|}$ and the identity is satisfied only for odd m [55]. This remains true for real-valued m as no value of $m \in \mathbb{R}$ satisfies both identities simultaneously (corresponding to the plus and minus signs). Therefore, the ESNM is asymmetric over the symmetry transformation given by Eq. (4) for all values of m, except when m is an odd integer number.

To observe the effect of different values of m on the system, we set the parameter values $a = 0.805$, $b = 0.597$, and $c = 0.005$ and construct the phase space for eight different values of m (Fig. 1). For these parameters, the shearless curve has already been broken [55]. Fig. 2 shows the magnifications around the colored dashed boxes in Fig. 1. For odd m [Figs. 1(a) and 1(e)], the twin island chain scenario is observed: the islands have the same size and inner structure and the symmetry transformation [Eq. (4)] maps the red dots [Figs. 2(a_1) and 2(e_1)] into the blue dots [Figs. 2(a_2) and 2(e_2)] and vice versa. However, for even m [Figs. 1(b)

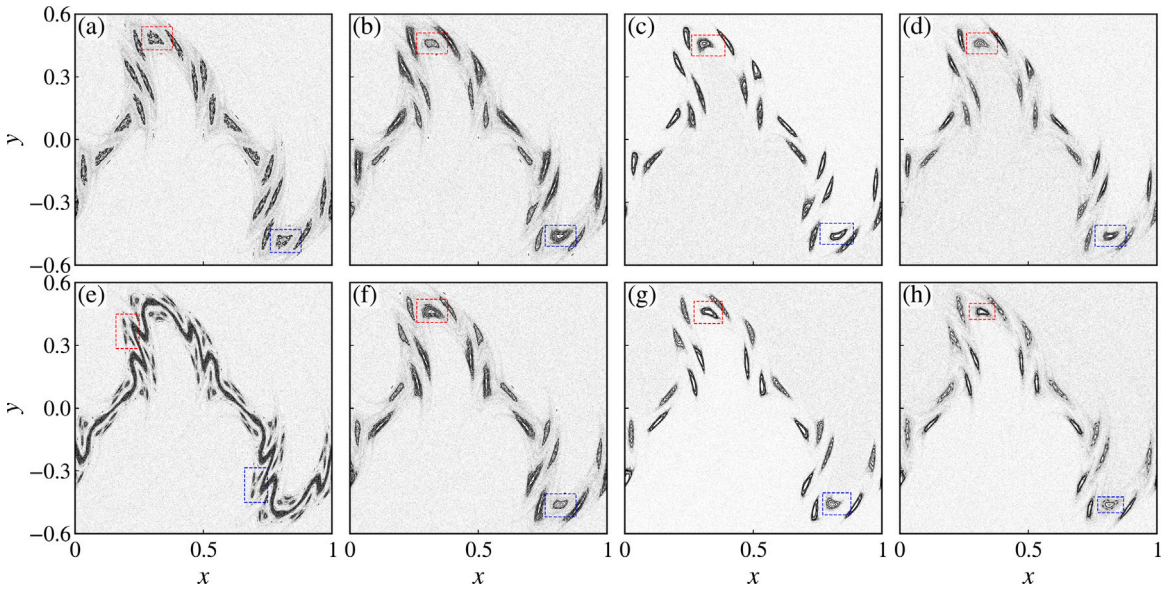

Fig. 1. Phase space of the ESNM [Eq. (3)] for $a = 0.805$, $b = 0.597$, $c = 0.005$ with (a) $m = 1$, (b) $m = 2$, (c) $m = 0.5$, (d) $m = 1.5$, (e) $m = -1$, (f) $m = -2$, (g) $m = -0.5$, and (h) $m = -1.5$. The dashed boxes correspond to the magnifications shown in Fig. 2.

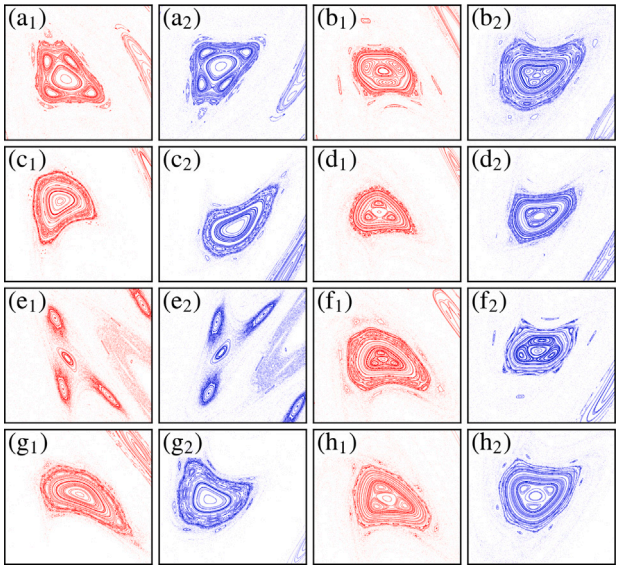

Fig. 2. Magnification of the dashed boxes shown in Fig. 1 with (a) $m = 1$, (b) $m = 2$, (c) $m = 0.5$, (d) $m = 1.5$, (e) $m = -1$, (f) $m = -2$, (g) $m = -0.5$, and (h) $m = -1.5$. The colors of the points match the colors of the dashed boxes.

and 1(f)] and for real valued m [Figs. 1(c), 1(d), 1(g), and 1(h)], the island chains are no longer twins: the size of the islands is different, and the period of the satellite islands changes. The inner structure of the islands is also different. These differences are more clearly visible in Fig. 2.

Therefore, the twin island chain scenario in the ESNM is related to whether the symmetry transformation given by Eq. (4) holds or not [55] and the structure of the island chains affects the transport of chaotic particles in phase space [52–54,59]. The effect of even or odd m on the transport in the ESNM has already been reported by Mugnaine et al. for short times [55] and the authors demonstrated the emergence of a Hamiltonian ratchet effect for even values of m due to the symmetry breaking. Thus, in Section 3, we investigate the role of real-valued m on the transport of chaotic particles in phase space for longer times.

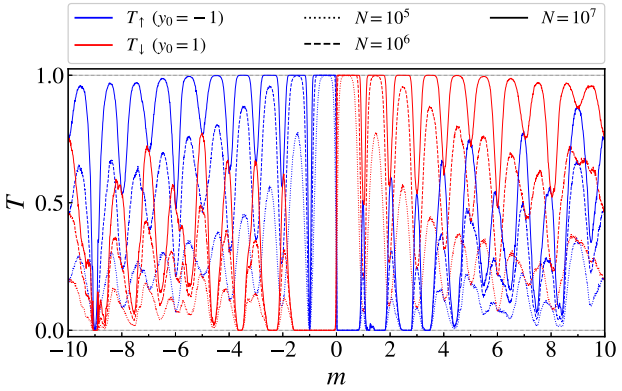

Fig. 3. The transmissivity [Eq. (6)] as a function of m. The transmissivity is defined as the number of trajectories, initially at $y_0 = 1$ ($y_0 = -1$) that cross the line $y = -1$ ($y = 1$), i.e., it is the number of trajectories that cross the central structure, divided by the total number of trajectories. We have considered an ensemble of $M = 1 \times 10^4$ chaotic initial conditions and iterated each one of for at most (dotted curves) $N = 1 \times 10^5$, (dashed curves) $N = 1 \times 10^6$, and (full curves) $N = 1 \times 10^7$.

3. Transport and manifolds

In this section, we investigate the mechanism behind the transport of chaotic trajectories across the central island structure shown in Fig. 1. Unless stated otherwise, the parameters are fixed at $a = 0.805$, $b = 0.597$, and $c = 0.005$. For these values, the dominant features influencing transport are two chains of period-11 stability islands, representing the primary resonances. As discussed in Section 2, the properties of the two island chains can either match or differ depending on the value of m. Previous studies have shown that, over short timescales, asymmetries between the upper and lower chains lead to an unbalanced stickiness effect, i.e., the chaotic trajectories stick differently in the upper and lower islands, which in turn produces different transport behaviors [55,60].

Therefore, we measure the transport across the central structure in both directions, upward and downward, using the transmissivity, T, as defined in Ref. [52]. The transmissivity quantifies the fraction of trajectories, initially located above or below the central structure, that successfully cross to the opposite side:

$$T_{\uparrow\downarrow} = \frac{\mathcal{N}_{\uparrow\downarrow}}{M}, \tag{6}$$

where $\mathcal{N}_{\uparrow\downarrow}$ is the number of trajectories, initially at $y_0 = -1$ and $y_0 = 1$, that reach the lines $y = 1$ and $y = -1$, respectively, and M is the total number of initial conditions. We consider an ensemble of $M = 1 \times 10^4$ chaotic initial conditions randomly distributed in $(x, y) = [0, 1) \times \pm 1$. We evolve each trajectory to at most $N = 1 \times 10^6$ iterations and if the trajectory reaches the opposite side of the structure, either $y = 1$ for $y_0 = -1$ or $y = -1$ for $y_0 = 1$, we stop the simulation and initialize another trajectory. We repeat this procedure until the whole ensemble is exhausted. From this ensemble, we calculate the transmissivity [Eq. (6)] as a function of m in the interval $m \in [-10, 10]$ with a step of $\Delta m = 0.01$ (Fig. 3).

The transmissivity plot shown in Fig. 3 displays an oscillatory behavior with high and low values in both upward and downward directions. However, it is noteworthy that for positive values of m, downward transmission is dominant ($T_\downarrow > T_\uparrow$), while for negative m, upward transmission prevails ($T_\uparrow > T_\downarrow$). However, the greater the number of iterations, the larger is the transmissivity, which indicates that for infinite times, when transport occurs in both directions, $T_{\uparrow\downarrow} \to 1$. Another interesting point is that for integer values of m, the red and blue curves intersect, indicating the presence of transport in a symmetric manner. This transport symmetry does not hold for non-integer values of m, where transmissivity tends to prevail in one direction depending on the sign of m. This asymmetry could also be verified using the net flux, introduced in Refs. [2,3] and reviewed in Ref. [40].

Therefore, the value of m plays a crucial role in achieving directed transport, i.e., a larger transmissivity in one direction than in the other for the same time scale. Additionally, whether m is rational or irrational does not influence the transport of chaotic trajectories (not shown). However, phase spaces alone do not provide sufficient information to understand the preference for this directionality. To shed light on the mechanisms behind this preference, we introduce Figs. 4, 5, and 6, which combines three important pieces of information as follows: (i) the upper (lower) chain of islands, marked in orange (blue); (ii) the position of the upper (lower) hyperbolic points, indicated by orange (blue) dots; and (iii) the upper (lower) stable manifold, represented by a fuchsia (light blue) line, and the upper (lower) unstable manifold, by a red (dark blue) line. Let $\mathbf{H} \in \mathbb{R}^2$ be a point on a hyperbolic periodic orbit of period $p > 1$, such that $\mathcal{M}^p(\mathbf{H}) = \mathbf{H}$ and let the periodic orbit be denoted by $\mathcal{O} = (\mathbf{H}, \mathcal{M}(\mathbf{H}), \ldots, \mathcal{M}^{p-1}(\mathbf{H}))$. The stable manifold of $\mathcal{O}$, $W_s(\mathcal{O})$, is defined as the set of all points in $\mathbb{R}^2$ that asymptotically approach the orbit $\mathcal{O}$ forward in time under the application of the mapping $\mathcal{M}$. The unstable manifold of $\mathcal{O}$, $W_u(\mathcal{O})$, similarly, is the set of all points in $\mathbb{R}^2$ that asymptotically approach the orbit $\mathcal{O}$ backward in time under the application of the mapping $\mathcal{M}$. Mathematically,

$$\begin{aligned} W_s(\mathcal{O}) &= \left\{ (x, y) \in \mathbb{R}^2 \mid \lim_{n \to \infty} \mathrm{dist}(\mathcal{M}^n(x, y), \mathcal{O}) = 0 \right\}, \\ W_u(\mathcal{O}) &= \left\{ (x, y) \in \mathbb{R}^2 \mid \lim_{n \to \infty} \mathrm{dist}(\mathcal{M}^{-n}(x, y), \mathcal{O}) = 0 \right\}. \end{aligned} \tag{7}$$

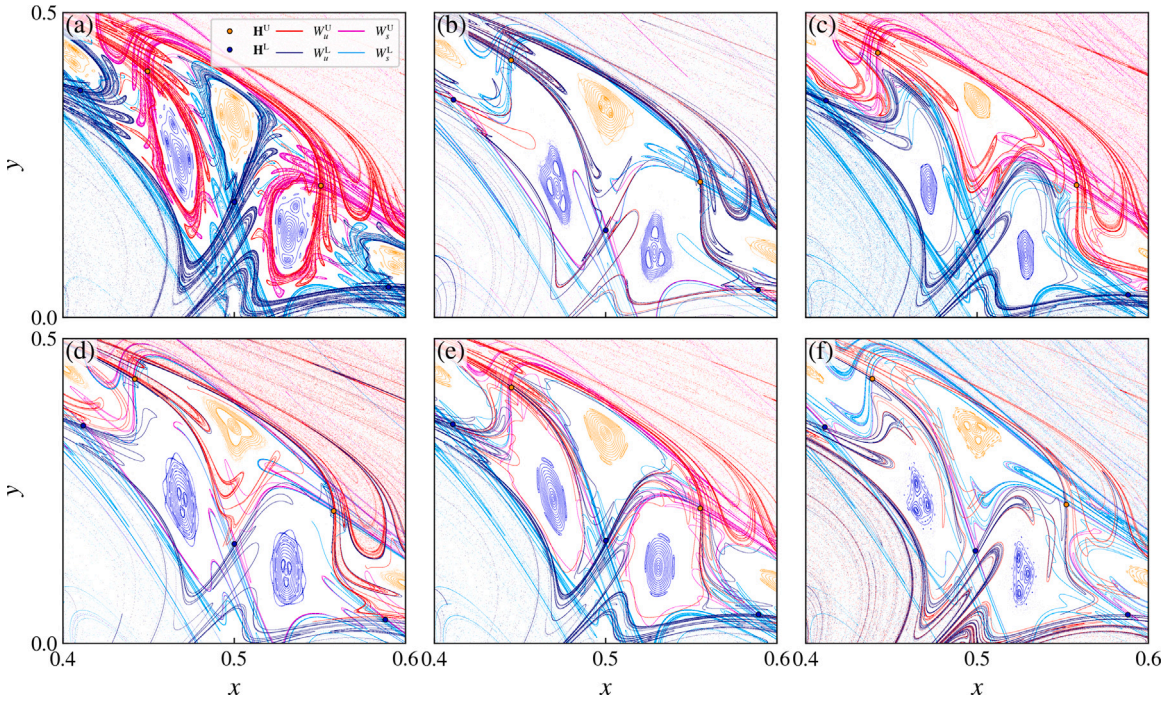

Fig. 4. The manifold configuration for (a) $m = 1$, (b) $m = 2$, (c) $m = 3$, (d) $m = -2$, (e) $m = -3$, and (f) $m = 3.5$. The orange (blue) dots correspond to the upper (lower) hyperbolic points. The red (dark blue) curve is the unstable manifold of the upper (lower) hyperbolic points and the fuchsia (light blue) curve is the stable manifold of the upper (lower) hyperbolic points. In all cases of values of m, the upper and lower manifolds form an intercrossing. (For interpretation of the references to color in this figure legend, the reader is referred to the web version of this article.)

To calculate the manifolds shown in Figs. 4, 5, and 6, we proceed as follows [82]: We begin by selecting one of the $p = 11$ points of the orbits and calculate its eigenvectors, $\mathbf{v}_s$ (stable) and $\mathbf{v}_u$ (unstable). Next, we choose 10^5 initial conditions uniformly distributed along the unstable eigenvector $\mathbf{v}_u$ and its negative counterpart $-\mathbf{v}_u$, within a distance of 10^{-6} from the point of the periodic orbit. We then calculate the trajectories of each of these points. This results in the unstable manifold shown in red for the upper chain of hyperbolic points and in dark blue for the lower chain of hyperbolic points. The stable manifold is obtained similarly using the stable eigenvector $\mathbf{v}_s$, its negative counterpart $-\mathbf{v}_s$, and the backward map instead. The stable manifold is shown in fuchsia for the upper chain of hyperbolic points and in light blue (cyan) for the lower chain of hyperbolic points. All of these calculations, including the determination of the periodic orbits, are performed in Fortran using quadruple precision (32-bit floating-point arithmetic).

Firstly, we analyze five cases of integer values of m, which are represented in Fig. 4(a)–4(e). In this case, we have three odd and two even values of m shown in panels (a), (c), (e) and (b), (d), respectively. We analyze the behavior of the stable and unstable manifolds. In all cases, regardless of the parity or sign of m, it is observed that the lower stable manifold (light blue) mutually crosses the upper unstable manifold (red) and that the lower unstable manifold (dark blue) mutually crosses the upper stable manifold (fuchsia), forming *heteroclinic* tangles between the upper and lower manifolds. These heteroclinic crossings occur symmetrically, i.e., in both the upward and downward directions, resulting in a *symmetric intercrossing*, even though the symmetry transformation [Eq. (4)] is not always valid. A direct consequence of these intercrossings is the transmissivity observed in Fig. 3. For integer values of m, we obtain non-zero transport across the central structure due to the intercrossings, which create channels through which trajectories cross the island chains. However, even in the absence of symmetry between the upper and lower islands for even m, the intercrossings remain essentially symmetric, i.e., present in both sides of the island chain, resulting in almost zero directed transport. An interesting change occurs in the case $m = 3.5$, shown in Fig. 4(f). While intercrossings between the upper and lower manifolds are still present, the upper (red) and lower (dark blue) unstable manifolds lose their symmetry. Specifically, the upper unstable manifold extends into the lower region of the phase space, whereas the inverse does not occur. Thus, directed transport cannot be ruled out in this case.

A new transport route emerges when, instead of considering only integer values of m, we will now examine in more detail the non-integer cases. Fig. 5 shows six cases for non-integer values of m, both positive and negative, shown in the upper and lower panels, respectively. We begin by focusing on the upper unstable manifold, represented by the red curve. It is notable that in the upper panels (positive values of m), this upper unstable manifold approaches the lower hyperbolic fixed point and even exhibits several intersections with the lower stable manifold, shown by the light blue curve. On the other hand, the lower unstable manifold, represented by the dark blue curve, does not cross with the upper stable manifold, depicted by the fuchsia curve. This

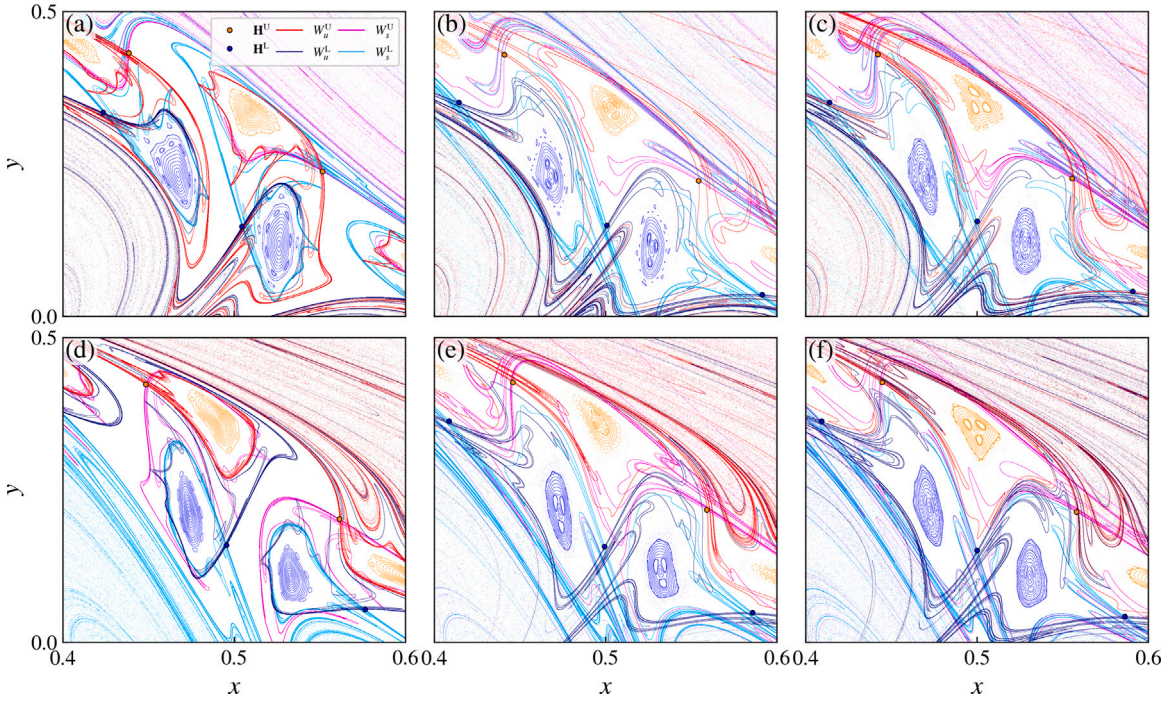

Fig. 5. The manifold configuration for (a) $m = 0.5$, (b) $m = 1.5$, (c) $m = 2.5$, (d) $m = -0.5$, (e) $m = -1.5$, and (f) $m = -2.5$. The orange (blue) dots correspond to the upper (lower) hyperbolic points. The red (dark blue) curve is the unstable manifold of the upper (lower) hyperbolic points and the fuchsia (light blue) curve is the stable manifold of the upper (lower) hyperbolic points. In the top row [(a)–(c)], only the heteroclinic point generated from the crossing between the upper unstable manifold (red curve) and the lower stable manifold (light blue curve) is present, forming an upward intercrossing. While in the bottom row [(d)–(f)] only the heteroclinic point generated from the crossing between the lower unstable manifold (dark blue curve) and the upper stable manifold (fuchsia curve) is present, forming a downward intercrossing. (For interpretation of the references to color in this figure legend, the reader is referred to the web version of this article.)

indicates a different scenario from the previous cases in Fig. 4(a)–4(e), we now observe an asymmetry in the manifold intersections, corresponding to an *asymmetric intercrossing*.

Next, analyzing the lower panels of Fig. 5 (negative values of m), we observe an opposite scenario. Now, the lower unstable manifold intersects the upper stable manifold and reaches the upper region of the phase space. In turn, the upper unstable manifold does not cross the lower stable manifold, and once again we observe an *asymmetric intercrossing*. However, it is important to highlight that although all cases in Fig. 5 involve asymmetric intercrossing, in the upper panels there is a crossing from the upper unstable manifold to the lower region, which we refer to as a *downward intercrossing*. In contrast, the lower panels exhibit the opposite configuration, generating what we define as an *upward intercrossing*. The breaking of symmetry and the existence of these two new types of intercrossings, upward and downward, are the reasons for the high and asymmetric transmissivity observed for non-integer values of m in Fig. 3. For positive non-integer m, there is a predominance of downward intercrossing, which results in negative directed transport. Conversely, for negative non-integer m, upward intercrossing occurs, producing positive transport.

In addition to the presence of intercrossing, we report two other possibilities in Figs. 6(a) and 6(b), corresponding to an *intracrossing* and the presence of a shearless curve, respectively. Starting with the case shown in Fig. 6(a), unlike the intercrossing case, which is dominated by heteroclinic manifold crossings, the intracrossing is characterized by *homoclinic* crossings. This is observed when taking the upper hyperbolic fixed point (orange dot) the upper stable and unstable manifolds do not intersect with the lower manifolds. The same reasoning holds if we instead take the lower hyperbolic fixed point (dark blue dot) as a reference. Thus, asymmetric or symmetric intercrossings are ruled out, and only intracrossing is present. A direct consequence of this configuration for $m = -1$ is an abrupt decrease in transmissivity, as observed in Fig. 3. In other words, the intercrossing channels that facilitate transport across the island chains are absent, significantly hindering the crossing of trajectories. In Fig. 7(a), to analyze the long-term behavior, we calculate the transmissivity in the specific case of $m = -1$ over extended iteration times. The transmissivity starts to be nonzero after nearly one million iterations, and even then, only a very small fraction of trajectories manages to cross. In this sense, we say that this intracrossing case forms a persistent partial barrier, limiting the system's transmissivity.

In contrast, Fig. 6(b) shows that for the case $m = -9$, a shearless invariant curve emerges, represented in green. To confirm that this structure is indeed a shearless invariant curve, we compute the rotation number $\omega(y)$. The rotation number is an irrational number for a quasiperiodic orbit and a rational number for a periodic one. For chaotic orbits, the rotation number is not defined.

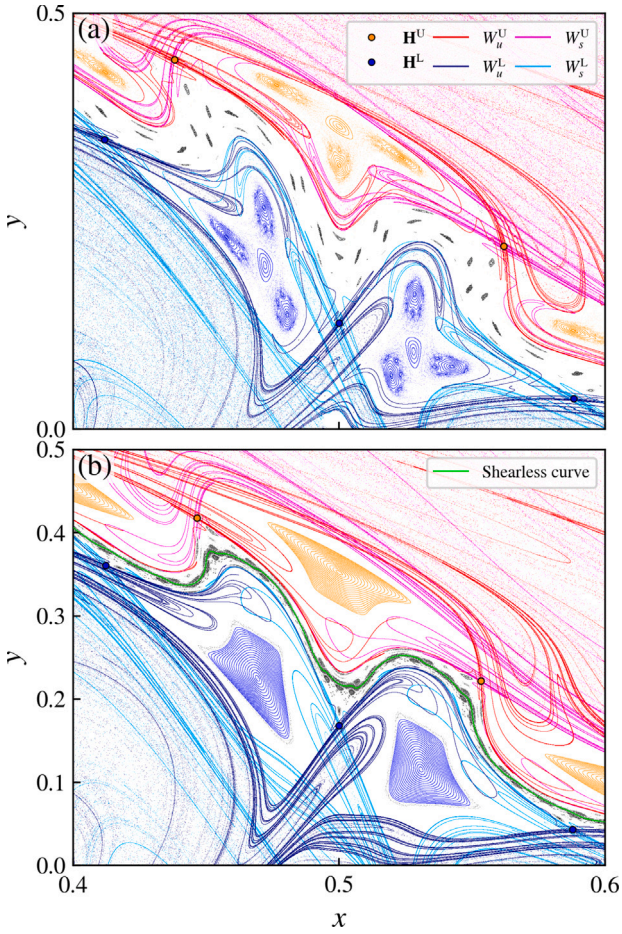

Fig. 6. The manifold configurations for (a) $m = -1$ and (b) $m = -9$. In both cases, the manifolds associated with the period-11 hyperbolic points do not cross. These correspond to the cases where transmissivity drops to zero in Fig. 3. For $m = -9$, a shearless curve [green line in (b)] acts as a complete transport barrier. In contrast, for $m = -1$, no such barrier exists. Instead, a set of smaller islands between the period-11 chains slows down transport without fully preventing it, and the upper, and lower manifolds form intracrossings. (For interpretation of the references to color in this figure legend, the reader is referred to the web version of this article.)

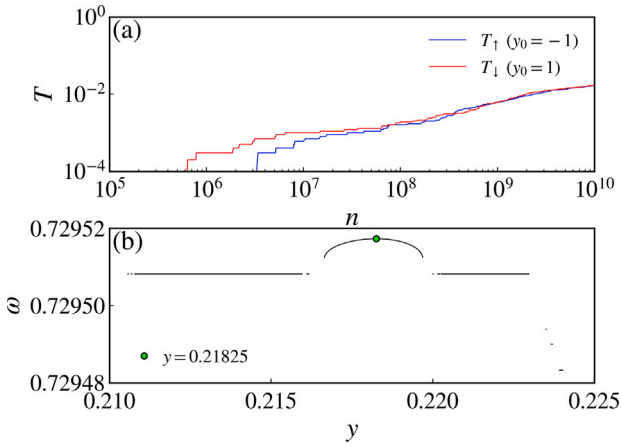

Fig. 7. (a) The transmissivity as a function of time for an ensemble of $M = 1 \times 10^4$ chaotic initial conditions initially at $y_0 = -1$ (blue curve) and at $y_0 = 1$ (red curve) with $m = -1$. (b) The rotation number [Eq. (8)] as a function of y calculated on the line $x = 0.5$. (For interpretation of the references to color in this figure legend, the reader is referred to the web version of this article.)

It can be computed with either one of the following expressions:

$$\omega_1(y) = \frac{1}{N}\sum_{n=1}^{N}(x_{n+1} - x_n) \bmod 1,$$
$$\omega_2(y) = \frac{1}{N}\sum_{n=1}^{N}\Omega(y_{n+1}) = \frac{1}{N}\sum_{n=1}^{N}a(1 - y_{n+1}^2). \tag{8}$$

In our case, $x \in [0, 1)$ and when we extend x to $\mathbb{R}$, both expressions become equal. However, we cannot extend x as this extension yields a different mapping due to the discontinuity and aperiodicity we have previously discussed. Nevertheless, both ω_1 and ω_2 converge to the same value for regular orbits. Therefore, we fix $x_0 = 0.5$ and vary the value of y and calculate $\omega_1(y)$ and $\omega_2(y)$ for $N = 1 \times 10^8$ iterations using the weighted Birkhoff average method described in Ref. [83] instead of computing simply the Birkhoff average as in Eq. (8). We check the convergence of the rotation number for every (x_0, y) as $|\omega_1 - \omega_2| < 10^{-15}$. If this requirement is satisfied, we plot the rotation number, otherwise, we discard it [Fig. 7(b)].

We observe two plateaus in the profile of $\omega(y)$, indicating two stability islands, and between these two plateaus, we observe a nonmonotonic behavior of $\omega(y)$. The extreme point, denoted by the green dot, indicates the position of the shearless curve. The shearless curve acts as a complete transport barrier and its presence leads to zero transmissivity, as shown in Fig. 3 for $m = -9$. In this case, regardless of the number of iterations, the transport barrier remains, fully preventing trajectory crossings.

4. Conclusions

In this paper, we have examined the transport mechanisms inherent to the extended standard nontwist map (ESNM). Additionally, we have explored the impact of incorporating a secondary frequency for both integer and non-integer wavenumbers. The symmetry transformation of the ESNM is preserved exclusively for odd integer wavenumbers. For non-integer wavenumbers, the mapping becomes discontinuous on the cylinder $(x, y) \in [0, 1) \times \mathbb{R}$. One possible workaround is to consider a larger cylinder: if $m = p/q$ with p and q integers, the system can instead be studied on the extended domain $x \in [0, q)$ where it is continuous. This approach, however, results in a dynamics that are similar but not equivalent to that on the original domain. A detailed analysis of this alternative formulation together with a deeper study on the effect of a quasiperiodic forcing in our system will be presented in a forthcoming paper.

We have demonstrated how the dependence on wavenumber values affects the existence of islands, as well as the breakdown of twin island scenarios. The symmetry of the system also plays a fundamental role in the configuration of the manifolds, and consequently, in the resulting transport behavior. We have applied the dynamic transmissivity quantifier in two channels to detect upward and downward transport. Our results show that transport is highly sensitive to the wavenumber value. However, in both even and odd cases, despite the symmetry transformation existing only for odd values, the upward and downward transport remains equivalent for long iterations time, meaning that the net directed transport is zero for the same time scale. This behavior arises from the heteroclinic entanglement of the manifolds associated with the upper and lower islands, which form transport channels. Nevertheless, due to their symmetry, i.e., the heteroclinic crossings occur in both the upward and downward directions, there is no preferred direction of transport. This crossing symmetry does not hold for some non-integer wavenumbers. For some positive non-integer wavenumbers, we have observed a configuration of the manifolds that leads to predominant downward transport for a fixed time scale, referred to as downward intercrossing. Conversely, for negative non-integer wavenumbers, the upward intercrossing scenario occurs, resulting in a net positive (upward) transport.

In addition to the symmetric and asymmetric intercrossing scenarios, we have identified another possible configuration involving homoclinic manifold crossings between the upper and lower island chains, referred to as intracrossing. Although this configuration does not correspond to an invariant curve that separates the system into two distinct regions, it functions as a partial yet persistent transport barrier, preventing upward or downward crossings over extremely long time scales. We have also found that, for specific values of the wavenumber, a shearless invariant curve emerges. This structure acts as a complete transport barrier, effectively prohibiting transport over infinite time scales. The effect of the second perturbation strength has already been studied in Ref. [55] for different integer wavenumber m. We intend to study in more details the influence of the wavenumber on the existence of the shearless curve in a future work.

In summary, our results indicate that the extended standard nontwist map exhibits a new range of transport mechanisms arising from the complexity of the crossings between its manifolds. We presented scenarios involving total barriers, partial barriers, as well as symmetric and asymmetric transport. Our findings suggest that these mechanisms may represent a general transport phenomenon, with the potential to influence the dynamical properties of a broader class of nontwist systems.

CRediT authorship contribution statement

Matheus Rolim Sales: Writing – review & editing, Writing – original draft, Visualization, Validation, Software, Project administration, Methodology, Investigation, Formal analysis, Data curation, Conceptualization. **Michele Mugnaine:** Writing – review & editing, Writing – original draft, Visualization, Validation, Methodology, Investigation, Formal analysis, Data curation, Conceptualization. **Ana L.R. de Moraes:** Writing – review & editing, Writing – original draft, Visualization, Validation, Methodology, Investigation, Formal analysis, Data curation, Conceptualization. **Edson Denis Leonel:** Writing – review & editing, Writing – original draft, Visualization, Validation, Methodology, Investigation, Formal analysis, Data curation, Conceptualization. **Chris G.**

Antonopoulos: Writing – review & editing, Writing – original draft, Visualization, Validation, Methodology, Investigation, Formal analysis, Data curation, Conceptualization. **Iberê Luiz Caldas:** Writing – review & editing, Writing – original draft, Visualization, Validation, Supervision, Methodology, Investigation, Formal analysis, Data curation, Conceptualization. **José Danilo Szezech:** Writing – review & editing, Writing – original draft, Visualization, Validation, Supervision, Methodology, Investigation, Formal analysis, Data curation, Conceptualization.

Code availability

The source code to reproduce the results reported in this paper is freely available in the GitHub repository in Ref. [84].

Declaration of competing interest

The authors declare that they have no known competing financial interests or personal relationships that could have appeared to influence the work reported in this paper.

Acknowledgments

This work was supported by the National Council for Scientific and Technological Development (CNPq, Brazil), under Grant Nos. 301318/2019-0, 304616/2021-4, 304398/2023-3, and 309670/2023-3, and by the São Paulo Research Foundation (FAPESP, Brazil), under Grant Nos. 2019/14038-6, 2021/09519-5, 2023/08698-9, 2024/09208-8, 2024/14825-6, 2024/03570-7, 2024/03570-7, 2024/05700-5, and 2025/05453-0. We would also like to thank the 105GroupScience for fruitful discussions.

Data availability

I have shared the link to the GitHub repository in the Data Availability section.

References

[1] Lichtenberg AJ, Lieberman MA. Regular and chaotic dynamics. In: Applied mathematical sciences, vol. 38, Springer-Verlag; 1992.
[2] MacKay RS, Meiss JD, Percival IC. Stochasticity and transport in Hamiltonian systems. Phys Rev Lett 1984;52:697–700.
[3] MacKay RS, Meiss JD, Percival IC. Transport in Hamiltonian systems. Phys D: Nonlinear Phenom 1984;13(1):55–81.
[4] Efthymiopoulos C, Contopoulos G, Voglis N, Dvorak R. Stickiness and cantori. J Phys A: Math Gen 1997;30:8167.
[5] Contopoulos G. Orbits in highly perturbed dynamical systems. iii. nonperiodic orbits. Astron J 1971;76:147.
[6] Meiss JD, Cary JR, Grebogi C, Crawford JD, Kaufman AN, Abarbanel HDI. Correlations of periodic, area-preserving maps. Physica D 1983;6(3):375–84.
[7] Karney CFF. Long-time correlations in the stochastic regime. Phys D: Nonlinear Phenom 1983;8(3):360–80.
[8] Chirikov BV, Shepelyansky DL. Correlation properties of dynamical chaos in Hamiltonian systems. Phys D: Nonlinear Phenom 1984;13(3):395–400.
[9] Meiss JD, Ott E. Markov-tree model of intrinsic transport in Hamiltonian systems. Phys Rev Lett 1985;55:2741–4.
[10] Meiss JD, Ott E. Markov tree model of transport in area-preserving maps. Phys D: Nonlinear Phenom 1986;20(2):387–402.
[11] Zaslavsky GM. Dynamical traps. Phys D: Nonlinear Phenom 2002;168–169:292–304, VII Latin American Workshop on Nonlinear Phenomena.
[12] Contopoulos G, Harsoula M. Stickiness in chaos. Int J Bifur Chaos 2008;18(10):2929–49.
[13] Cristadoro G, Ketzmerick R. Universality of algebraic decays in Hamiltonian systems. Phys Rev Lett 2008;100:184101.
[14] Contopoulos G, Harsoula M. Stickiness effects in conservative systems. Int J Bifurc Chaos 2010;20(07):2005–43.
[15] Afraimovich V, Zaslavsky GM. Fractal and multifractal properties of exit times and poincaré recurrences. Phys Rev E 1997;55:5418–26.
[16] Altmann EG, Motter AE, Kantz H. Stickiness in mushroom billiards. Chaos: Interdiscip J Nonlinear Sci 2005;15:033105.
[17] Altmann EG, Motter AE, Kantz H. Stickiness in Hamiltonian systems: From sharply divided to hierarchical phase space. Phys Rev E 2006;73:026207.
[18] Venegeroles R. Universality of algebraic laws in Hamiltonian systems. Phys Rev Lett 2009;102:064101.
[19] Abud CV, de Carvalho RE. Multifractality, stickiness, and recurrence-time statistics. Phys Rev E 2013;88:042922.
[20] Lozej Č. Stickiness in generic low-dimensional Hamiltonian systems: A recurrence-time statistics approach. Phys Rev E 2020;101:052204.
[21] Lai Y-C, Ding M, Grebogi C, Blümel R. Algebraic decay and fluctuations of the decay exponent in Hamiltonian systems. Phys Rev A 1992;46:4661–9.
[22] Altmann EG, Tél T. Poincaré recurrences and transient chaos in systems with leaks. Phys Rev E 2009;79:016204.
[23] Avetisov VA, Nechaev SK. Chaotic Hamiltonian systems: Survival probability. Phys Rev E 2010;81:046211.
[24] Dettmann CP, Leonel ED. Escape and transport for an open bouncer: Stretched exponential decays. Phys D: Nonlinear Phenom 2012;241(4):403–8.
[25] Livorati ALP, Georgiou O, Dettmann CP, Leonel ED. Escape through a time-dependent hole in the doubling map. Phys Rev E 2014;89:052913.
[26] Borin D, Livorati ALP, Leonel ED. An investigation of the survival probability for chaotic diffusion in a family of discrete Hamiltonian mappings. Chaos Solitons Fractals 2023;175:113965.
[27] Rolim Sales M, Borin D, da Costa DR, Szezech J, Danilo José, Leonel ED. An investigation of escape and scaling properties of a billiard system. Chaos: Interdiscip J Nonlinear Sci 2024;34:113122.
[28] Vivaldi F, Casati G, Guarneri I. Origin of long-time tails in strongly chaotic systems. Phys Rev Lett 1983;51:727–30.
[29] Lozej Č, Robnik M. Structure, size, and statistical properties of chaotic components in a mixed-type Hamiltonian system. Phys Rev E 2018;98:022220.
[30] Motter AE, de Moura APS, Grebogi C, Kantz H. Effective dynamics in Hamiltonian systems with mixed phase space. Phys Rev E 2005;71:036215.
[31] Sales MR, Mugnaine M, Viana RL, Caldas IL, Szezech JD. Unpredictability in Hamiltonian systems with a hierarchical phase space. Phys Lett A 2022;431:127991.
[32] de Oliveira JA, Dettmann CP, da Costa DR, Leonel ED. Scaling invariance of the diffusion coefficient in a family of two-dimensional Hamiltonian mappings. Phys Rev E 2013;87:062904.
[33] Harsoula M, Contopoulos G. Global and local diffusion in the standard map. Phys Rev E 2018;97:2.
[34] Livorati AL, Palmero MS, Díaz-I G, Dettmann CP, Caldas IL, Leonel ED. Investigation of stickiness influence in the anomalous transport and diffusion for a non-dissipative Fermi–Ulam model. Commun Nonlinear Sci Numer Simul 2018;55:225–36.
[35] Díaz GI, Palmero MS, Caldas IL, Leonel ED. Diffusion entropy analysis in billiard systems. Phys Rev E 2019;100:10.

[36] Zaslavskiĭ GM, Chirikov BV. Stochastic instability of non-linear oscillations. Sov Phys Uspekhi 1972;14:549.
[37] Zaslavsky GM, Edelman M, Niyazov BA. Self-similarity, renormalization, and phase space nonuniformity of Hamiltonian chaotic dynamics. Chaos: Interdiscip J Nonlinear Sci 1997;7:159–81.
[38] Zaslavsky G. Chaos, fractional kinetics, and anomalous transport. Phys Rep 2002;371(6):461–580.
[39] Zaslavsky GM. Hamiltonian chaos and fractional dynamics. USA: Oxford University Press; 2005.
[40] Meiss JD. Thirty years of turnstiles and transport. Chaos 2015;25:3.
[41] Mackay RS, Meiss JD, Percival IC. Resonances in area-preserving maps. Phys D: Nonlinear Phenom 1987;27(1):1–20.
[42] Easton RW. Transport through chaos. Nonlinearity 1991;4:583.
[43] del Castillo-Negrete D, Morrison PJ. Chaotic transport by Rossby waves in shear flow. Phys Fluids A: Fluid Dyn 1993;5:948–65.
[44] Delshams A, de la Llave R. KAM theory and a partial justification of Greene's criterion for nontwist maps. SIAM J Math Anal 2000;31(6):1235–69.
[45] Howard JE, Hohs SM. Stochasticity and reconnection in Hamiltonian systems. Phys Rev A 1984;29:418–21.
[46] del Castillo-Negrete D, Greene JM, Morrison PJ. Area preserving nontwist maps: periodic orbits and transition to chaos. Phys D: Nonlinear Phenom 1996;91(1):1–23.
[47] del Castillo-Negrete D, Greene JM, Morrison PJ. Renormalization and transition to chaos in area preserving nontwist maps. Phys D: Nonlinear Phenom 1997;100(3):311–29.
[48] Howard JE, Humpherys J. Nonmonotonic twist maps. Phys D: Nonlinear Phenom 1995;80(3):256–76.
[49] Shinohara S, Aizawa Y. The breakup condition of shearless KAM curves in the quadratic map. Progr Theoret Phys 1997;97:379–85.
[50] Corso G, Oda G, Caldas IL. Minimizing chaos during the reconnection process. Chaos Solitons Fractals 1997;8(12):1891–900.
[51] Morrison PJ. Magnetic field lines, Hamiltonian dynamics, and nontwist systems. Phys Plasmas 2000;7:2279–89.
[52] Szezech Jr JD, Caldas IL, Lopes RL, Morrison PJ. Transport properties in nontwist area-preserving maps. Chaos: Interdiscip J Nonlinear Sci 2009;19:043108.
[53] Szezech JD, Caldas IL, Lopes SR, Morrison PJ, Viana RL. Effective transport barriers in nontwist systems. Phys Rev E 2012;86:036206.
[54] Mugnaine M, Mathias AC, Santos MS, Batista AM, Szezech JD, Viana RL. Dynamical characterization of transport barriers in nontwist Hamiltonian systems. Phys Rev E 2018;97:012214.
[55] Mugnaine M, Batista AM, Caldas IL, Szezech Jr JD, Viana RL. Ratchet current in nontwist Hamiltonian systems. Chaos: Interdiscip J Nonlinear Sci 2020;30:093141.
[56] Grime GC, Roberto M, Viana RL, Elskens Y, Caldas IL. Biquadratic nontwist map: a model for shearless bifurcations. Chaos Solitons Fractals 2023;169:113231.
[57] Grime GC, Roberto M, Viana RL, Elskens Y, Caldas IL. Shearless curve breakup in the biquadratic nontwist map. Chaos Solitons Fractals 2023;172:113606.
[58] Souza LC, Mathias AC, Haerter P, Viana RL. Basin entropy and shearless barrier breakup in open non-twist Hamiltonian systems. Entropy 2023;25:8.
[59] Mugnaine M, Caldas IL, Szezech JD, Viana RL, Morrison PJ. Shearless effective barriers to chaotic transport induced by even twin islands in nontwist systems. Phys Rev E 2024;110:044201.
[60] Rolim Sales M, Borin D, de Souza LC, Szezech Jr JD, Viana RL, Caldas IL, et al. Ratchet current and scaling properties in a nontwist mapping. Chaos Solitons Fractals 2024;189:115614.
[61] Simile Baroni R, de Carvalho RE. Lagrangian descriptors: The shearless curve and the shearless attractor. Phys Rev E 2024;109:024202.
[62] Simile Baroni R, de Carvalho RE, Szezech Junior JD, Caldas IL. Transport barriers and directed transport in the rational standard nontwist map. Phys Rev E 2025;111:034203.
[63] Grime GC, Caldas IL, Viana RL, Elskens Y. Effective transport barriers in the biquadratic nontwist map. Phys Rev E 2025;111:014219.
[64] Portela JSE, Caldas IL, Viana RL, Morrison PJ. Diffusive transport through a nontwist barrier in tokamaks. Int J Bifurc Chaos 2007;17(05):1589–98.
[65] Wurm A, Martini KM. Breakup of inverse golden mean shearless tori in the two-frequency standard nontwist map. Phys Lett A 2013;377(8):622–7.
[66] Chirikov BV. A universal instability of many-dimensional oscillator systems. Phys Rep 1979;52(5):263–379.
[67] Lieberman MA, Lichtenberg AJ. Stochastic and adiabatic behavior of particles accelerated by periodic forces. Phys Rev A 1972;5:1852–66.
[68] Silva JKLd, Ladeira DG, Leonel ED, McClintock PVE, Kamphorst SO. Scaling properties of the Fermi-Ulam accelerator model. Braz J Phys 2006;36:700–7.
[69] Leonel ED. Phase transition in dynamical systems: Defining classes of universality for two-dimensional Hamiltonian mappings via critical exponents. Math Probl Eng 2009;2009(1):367921.
[70] de Oliveira JA, Bizão RA, Leonel ED. Finding critical exponents for two-dimensional Hamiltonian maps. Phys Rev E 2010;81:046212.
[71] Leonel ED, Yoshida M, de Oliveira JA. Characterization of a continuous phase transition in a chaotic system. Europhys Lett 2020;131:20002.
[72] Aguilar-Sánchez R, Leonel ED, Méndez-Bermúdez JA. Dynamical properties of a dissipative discontinuous map: A scaling investigation. Phys Lett A 2013;377(44):3216–22.
[73] Perre RM, Carneiro BP, Méndez-Bermúdez JA, Leonel ED, de Oliveira JA. On the dynamics of two-dimensional dissipative discontinuous maps. Chaos Solitons Fractals 2020;131:109520.
[74] de Oliveira JA, Perre RM, Méndez-Bermúdez JA, Leonel ED. Leaking of orbits from the phase space of the dissipative discontinuous standard mapping. Phys Rev E 2021;103:012211.
[75] Borgonovi F. Localization in discontinuous quantum systems. Phys Rev Lett 1998;80:4653–6.
[76] Borgonovi F, Conti P, Rebuzzi D, Hu B, Li B. Cantori and dynamical localization in the bunimovich stadium. Phys D: Nonlinear Phenom 1999;131(1):317–26, Classical Chaos and its Quantum Manifestations.
[77] Ashwin P, Fu X-C, Terry JR. Riddling and invariance for discontinuous maps preserving Lebesgue measure. Nonlinearity 2002;15:633.
[78] Gutkin E. Billiards in polygons. Physica D 1986;19(3):311–33.
[79] Grebogi C, Ott E, Pelikan S, Yorke JA. Strange attractors that are not chaotic. Phys D: Nonlinear Phenom 1984;13:261–8.
[80] Romeiras FJ, Ott E. Strange nonchaotic attractors of the damped pendulum with quasiperiodic forcing. Phys Rev A 1987;35:4404–13.
[81] Mathias AC, Mugnaine M, Santos MS, Szezech JD, Caldas IL, Viana RL. Fractal structures in the parameter space of nontwist area-preserving maps. Phys Rev E 2019;100:052207.
[82] Hobson D. An efficient method for computing invariant manifolds of planar maps. J Comput Phys 1993;104(1):14–22.
[83] Sander E, Meiss JD. Birkhoff averages and rotational invariant circles for area-preserving maps. Phys D: Nonlinear Phenom 2020;411:132569.
[84] Rolim Sales M. mrolims/transport-noninteger-wavenumber. 2025.